NACE INTERNATIONAL | CORROSION 2018 Conference & Expo

Effect of Flow and Steel Microstructure on the Formation of Iron Carbonate

M. Di Bonaventura,[1] B. Brown, M. Singer and S. Nesic
Institute for Corrosion and Multiphase Technology
Department of Chemical and Biomolecular Engineering
Ohio University, Athens, OH 45701, USA

ABSTRACT

Iron carbonate ($FeCO_3$) is a protective layer that can form on the surface of the steel as a by-product of CO_2 corrosion. This layer acts as a barrier, thus slowing down further corrosion. Temperature, CO_2 partial pressure and pH are the main environmental parameters controlling $FeCO_3$ properties. However, the combined effects of flow and material microstructure on the formation of $FeCO_3$ have not been well documented. In this research, two materials were used to determine the effect of microstructure on the formation of iron carbonate: an annealed low alloy carbon steel (0.05 wt.% C), formally API[†] 5L X65, with ferrite and iron carbide (Fe_3C) precipitates microstructure and UNS[‡] G10180 (0.18 wt.% C) with either a ferritic-pearlitic or a tempered martensitic microstructure. $FeCO_3$ formation and retention of Fe_3C on the steel surface were investigated in experiments in a three-electrode glass cell under controlled water chemistry conditions. Experiments were performed using two different flow rotational speeds and lasted five days. SEM, EDS and XRD analyses of specimen surface after exposure provided corrosion product characterization. The experimental results clearly indicated an existence of a critical shear stress, above which $FeCO_3$ could not nucleate on the steel surface. In addition, the steel microstructure, rather the carbon content, had a strong effect on the results with the ferritic-pearlitic steel clearly favoring $FeCO_3$ precipitation.

Key words: CO_2 corrosion, flow, iron carbide, iron carbonate, microstructure, shear stress

INTRODUCTION

$FeCO_3$ is the commonest corrosion product that can form on the surface of mild steel as a by-product of the CO_2 corrosion process. This $FeCO_3$ layer slows down further corrosion by acting as a diffusion barrier, preventing corrosive species from reaching the steel surface and by blocking the steel surface

---

[1] Current affiliation: BP America, 501 Westlake Park Blvd, Houston, TX 77079, USA
[†] American Petroleum Institute (API), 1220 L St. NW, Washington, DC 20005.
[‡] Unified Numbering System for Metals and Alloys (UNS). UNS numbers are listed in Metals & Alloys in the Unified Numbering System, 10th ed. (Warrendale, PA: SAE International and West Conshohocken, PA: ASTM International, 2004).

making iron dissolution more difficult. On the other hand, Fe_3C, known as cementite or iron carbide, is often classified as a "corrosion product" but it is originally found in the material's microstructure and, unlike $FeCO_3$, it is not precipitated on the steel surface. Rather, it represents the "leftover" portion of the steel structure, once the ferrite phase has been corroded away. The exposed Fe_3C can act as a diffusion barrier for ferrous and carbonate ions favoring localized conditions for formation of a $FeCO_3$ layer at the surface of the steel

Ambiguous results have been found in the literature with regards to what microstructure favors $FeCO_3$ precipitation, and no consensus has been reached. Dugstad, *et al.*, found that a ferritic-pearlitic microstructure did not yield to $FeCO_3$ formation as corrosion rates remained high.[1] Ochoa, *et al.*, found that both ferritic-pearlitic or quenched and tempered microstructures favored formation of a protective $FeCO_3$ layer.[2]

Farelas[3] studied the influence of an Fe_3C layer on the formation of $FeCO_3$ by using two different steels and microstructures, API 5L X65 tempered martensite and UNS G10180 ferritic-pearlitic. Farelas concluded that formation of $FeCO_3$ is possible within the pores of the exposed "skeletal" Fe_3C layer, even when the bulk water chemistry conditions are unfavorable. Although Farelas's findings constituted a breakthrough in studying the role of Fe_3C, the author did not incorporate flow effects into his studies. Flow effects may play a major role in the formation of $FeCO_3$ within the pores of Fe_3C, since the Fe_3C layer is mechanically weak,[4] and thus susceptible to removal by flowing conditions. In a more recent study, Ieamsupapong[5] also found that the presence and characteristics of Fe_3C played a governing role in the formation of $FeCO_3$ on steel. His findings were similar to those of Farelas: Fe_3C acted as a diffusion barrier slowing diffusion of generated ferrous ions away from the surface, allowing formation of $FeCO_3$, using UNS G10180 ferritic-pearlitic steel, exposed to aqueous solutions at pH 5.4 to pH 6.0.[5]

Eliyan and Alfantazi, who found similar results to Farelas and Ieamsupapong, claimed that a ferritic-pearlitic microstructure was superior to other microstructures in regards to $FeCO_3$ formation due to the distribution of Fe_3C.[6] However, Berntsen stated that an exposed Fe_3C, obtained through pre-corrosion of the metal, did not have any beneficial impact in $FeCO_3$ formation,[7] contrary to what has been previously proposed.[3,5] This was due to the fact that most of the Fe_3C had spalled off during the experiments, while $FeCO_3$ formed. Although this study presented results at odds with what others found, these experiments, however, had iron carbonate saturation values in the range of 300-500, which likely facilitated $FeCO_3$ formation due to the high concentration of ferrous ions in solution.

High flow velocities, which are common in various field applications, have been postulated either to lead to partial mechanical removal of $FeCO_3$ layers or to impede the nucleation of $FeCO_3$ crystals on the steel surface altogether. Previous studies have shown that partial removal of $FeCO_3$ can lead to increase in metal loss and pitting – a very aggressive type of localized corrosion.[8] Thus, it is imperative to understand how this layer behaves and forms under a variety of environmental conditions, which can allow appropriate prediction of the corrosion rate, as well as $FeCO_3$ formation in flowing conditions. The overall objective of the current study is to identify if $FeCO_3$ formation is impeded by high flow velocities and if microstructural effects play a role here.

EXPERIMENTAL PROCEDURE

Experimental Setup

The set of experiments was performed using the experimental setup shown in Figure 1. The system consists of a three-electrode electrochemical glass cell, 2 L in volume, which can accommodate an impeller in the center of the glass cell to achieve controlled flow conditions. The advantage of the using an impeller with static specimen, instead of a rotating cylinder electrode (RCE) is that centrifugal forces found on a RCE, which can mechanically affect the formation of a corrosion product layer, are eliminated. At the same time multiple specimens can be used, while making sure that each specimen is exposed to well controlled and properly characterized mass transfer and shear stress conditions. In

these experiments, five flat metal specimens were located at a fixed height and distance from the impeller. One specimen was used for electrochemical measurements. The water chemistry (pH and ferrous ion concentration) in these experiments was controlled using ion exchange resin columns in order to maintain stable water chemistry throughout the experiments, to better mimic field conditions. The details of the procedure for using ion exchange resins to control water chemistry in electrochemical experiments have been explained in a previous publication by Zhong, *et al.*[9]

1. Ion exchange resin column for Fe^{2+} control
2. Timer
3. Pump (x2)
4. Condenser
5. Sample holder (x5)
6. Impeller
7. Hot plate
8. pH controller
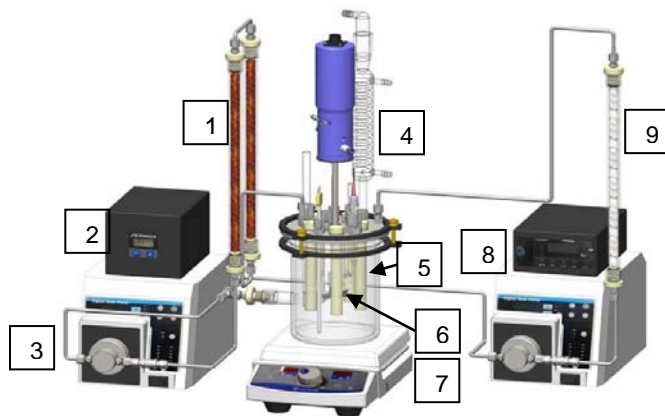9. Ion exchange resin column for pH control

Figure 1: Three-electrode glass cell with stable solution chemistry and controlled mass transfer setup

Experiments were conducted in a 1 wt.% NaCl electrolyte with initial saturation value with respect to $FeCO_3$ (S_{FeCO_3} = 10). This saturation value ensures steady $FeCO_3$ layer formation. Experiments were performed at two impeller speeds, 150 and 250 rpm. Equivalent pipeline velocities in a hypothetical 10" diameter pipe were also calculated by using equivalent mass transfer conditions. Wall shear stresses on the steel specimen surface were calculated via Computational Fluid Dynamics (CFD) simulations, as reported in Table 1. Duration of the experiments was five days, enabling sufficient Fe_3C to form, as indicated in previous experiments of this kind.[3,5] The other environmental conditions (pH 6.6, T = 80°C) were selected to ensure optimal corrosion product layer forming conditions, based on the literature review and analyses performed. Steel specimens were removed on the first, third, and last day for surface characterization to determine nature of corrosion product present (if any) and to do weight loss measurements. All experimental parameters are summarized in Table 1.

Materials

Three different materials and/or microstructures were tested: an annealed low allow carbon steel (originally API 5L X65) ferritic with Fe_3C precipitates (0.05 wt.% C), a ferritic-pearlitic UNS G10180, and a tempered martensitic UNS G10180. This facilitated testing the effect of microstructure and carbon content in flowing conditions. Table 2 shows all material compositions.

Specimen Preparation

The UNS G10180 tempered martensitic microstructure was obtained by quenching (heating at 950°C for 45 minutes and quenched in water for five minutes) and tempering (500°C for 2 hours). API 5L X65 specimens also underwent a thermal treatment (heating at 930°C for three hours) to match the grain size to that of UNS G10180. It is understood that the yield strength after a thermal treatment no longer matches the definition of an API 5L X65; however it will be referred to as API 5L X65 in this document for ease of following. Specimens were wet-polished with silicon carbide abrasive paper up to 600 grit in order to ensure uniform surface preparation prior to the start of experiments; this included rinsing with isopropyl alcohol and use of ultrasonication to remove any residue from the specimen surfaces. Specimens were dried with cold air before being mounted into a specimen holder. For the specimen used for electrochemical measurements, an insulated wire was soldered to its back prior to placement

in an epoxy mold; this permitted connection to a potentiostat. The mold was filled with an epoxy mixture to avoid any liquid entrainment therein that could cause galvanic corrosion.

Table 1
Experimental parameters used to study the effect of microstructure and flow on FeCO₃ formation

Experimental Setup	2L glass cell
Materials	UNS G10180 ferrite-pearlite UNS G10180 tempered martensite API 5L X65 ferrite with Fe_3C precipitates
Electrolyte	1 wt.% NaCl
pH	6.6 $\pm$ 0.03
Temperature	80^oC
Total Pressure	1 bar (10^5 Pa)
CO_2 Partial Pressure	0.53 bar (5.3 x 10^4 Pa)
[Fe^{2+}]	1 – 6 ppm
Saturation w.r.t. $FeCO_3$	10 – 30
Impeller Rotational Speeds	150 rpm and 250 rpm
Equivalent Pipeline Velocities in 10" pipe	0.4 m/s (150 rpm) and 0.6 m/s (250 rpm)
Shear Stresses	0.3 Pa (150 rpm) and 0.5 Pa (250 rpm)
Surface Analysis	SEM, XRD, and Cross-Section
Electrochemical Measurements	OCP and LPR

Table 2
Chemical composition of API 5L X65 (wt.%) and UNS G10180 (wt.%)

API 5L X65 mild steel (balance Fe)						
C	Mn	Nb	P	S	Ti	V
0.05	1.51	0.03	0.004	<0.001	0.01	0.04

UNS G10180 (balance Fe)									
Al	As	C	Co	Cr	Cu	Mn	Mo	Nb	Ni
0.008	0.006	0.18	0.003	0.12	0.18	0.75	0.020	0.002	0.065
P	S	Sb	Si	Sn	Ti	V	W	Zn	Zr
0.011	0.021	0.009	0.16	0.009	0.002	0.003	0.014	0.004	0.003

Electrochemical Measurements

A Gamry[§] potentiostat was used for electrochemical and potential measurements. The working electrode was polarized ±5 mV versus the open circuit potential using a scan rate of 0.125 mV/s for Linear Polarization Resistance (LPR) measurements. The B value that was used was 26 mV/decade[3,5,10,11] obtained from the literature as being typical for low temperature CO_2 corrosion of mild steel. The polarization resistance from LPR measurements was used to calculate the current density (i_{corr}, A/cm^2) and in turn the corrosion rate in millimeters per year (mm/yr) using the Stern-Geary Equation (1)[1,3,12,13] as follows:

$$\text{Corrosion rate (mm/yr)} = \frac{a i_{corr} \text{MW}}{\rho n F} \tag{1}$$

Where MW is the molecular weight of iron (g/mol), ρ is the density of iron (g/cm^3), n is the number of electrons involved in the electrochemical reaction, F is Faraday's constant, and a is a conversion factor to obtain corrosion rate in mm/yr units.

---

§ Trade Name

RESULTS AND DISCUSSION

UNS G10180 ferritic-pearlitic steel

Water Chemistry

Figure 2 shows the change of pH through the course of the experiments at each rotational speed. The average pH values for both rotational speeds was 6.60; pH was well controlled within a $\pm$ 0.03 deviation from the desired value of pH 6.60 for both rotational speeds. Figure 3 shows the comparison of Fe^{2+} concentration changes throughout the course of the experiments. The Fe^{2+} concentration was controlled using the ion exchange resin within 1 to 6 ppm, with the desired value being 2 ppm ($S(FeCO_3) \approx 10$). There was a slight increase of ferrous ion concentration for the 250 rpm experiment, but the average was maintained at a value of 3.5 ppm, which is still within the desired range.

	Min	Max	Avg
250 rpm (0.6 m/s)	6.58	6.60	6.60
150 rpm (0.4 m/s)	6.58	6.61	6.60
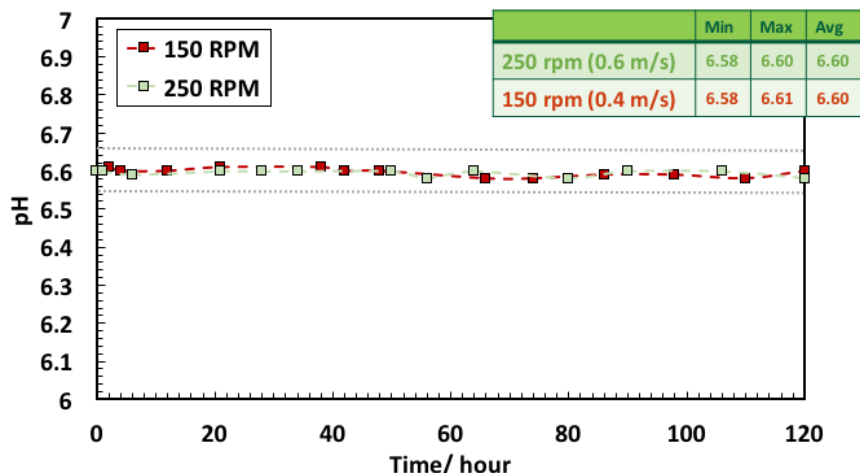
Figure 2: Comparison of pH over time for 150 rpm (V_{eq} = 0.4 m/s, 0.3 Pa) and 250 rpm (V_{eq} = 0.6 m/s, 0.5 Pa) experiments with UNS G10180 ferritic-pearlitic
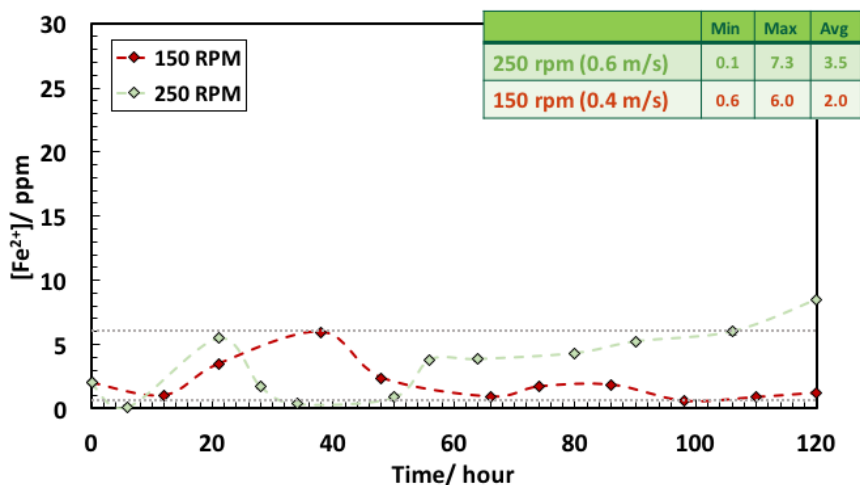

	Min	Max	Avg
250 rpm (0.6 m/s)	0.1	7.3	3.5
150 rpm (0.4 m/s)	0.6	6.0	2.0

Figure 3: Comparison of [Fe^{2+}] over time for 150 rpm (V_{eq} = 0.4 m/s, 0.3 Pa) and 250 rpm (V_{eq} = 0.6 m/s, 0.5 Pa) experiments with UNS G10180 ferritic-pearlitic

Corrosion Rates

Figure 4 shows the comparison of LPR corrosion rate over time for each rotational speed. It can be observed that initial corrosion rates start at about 2 mm/yr and increase over time, mainly because of

the buildup of Fe_3C.[**] Steels that contain the Fe_3C phase corroded at much faster rates than pure iron since Fe_3C acts as an active cathodic site.[4,6,14,15] In other words, the presence of Fe_3C increases the overall cathodic area which in turn promotes the dissolution of the iron.[4,6,7,14,15] This increase in corrosion rate over time has been termed as the 'active corrosion stage'.[3,5] For the 150 rpm experiment, the corrosion rate stopped increasing after the first day, and maintained a stable value until 65 h, when it decreased, reaching a low and steady value indicative of $FeCO_3$ formation. The stage where the corrosion rate is at a low and steady value has been commonly referred to as the 'pseudo-passivation' stage.[3,5] For the 250 rpm experiment, the corrosion rate increased for the first the 80 h. After that, the corrosion rate rapidly decreased, which is also indicative of $FeCO_3$ formation. The stage where the corrosion rate starts to decrease but has not yet reached a stable value is known as the 'nucleation and growth of $FeCO_3$' stage[3,5]. Repeats were not performed for UNS G10180 ferritic-pearlitic since the results matched the literature on this specific material and microstructure.[3,5]

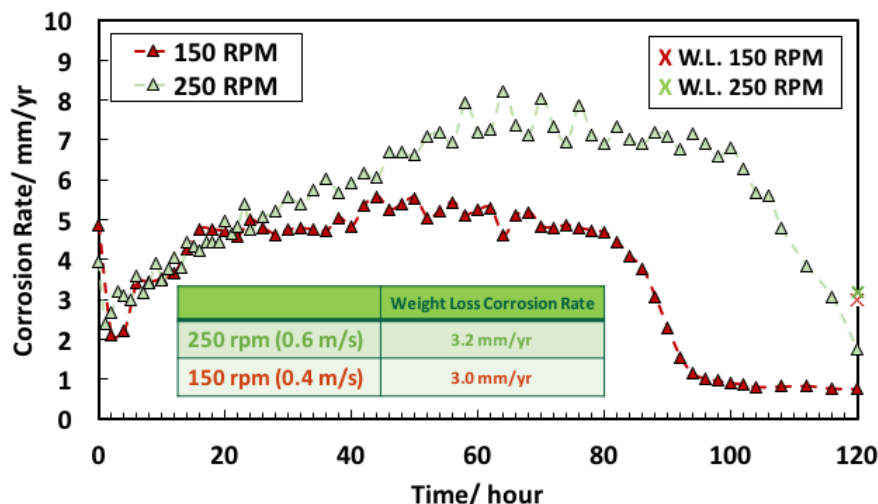|	Weight Loss Corrosion Rate
250 rpm (0.6 m/s)	3.2 mm/yr
150 rpm (0.4 m/s)	3.0 mm/yr

Figure 4: Comparison of LPR corrosion rate over time for 150 rpm (V_{eq} = 0.4 m/s, 0.3 Pa) and 250 rpm (V_{eq} = 0.6 m/s, 0.5 Pa) experiments with UNS G10180 ferritic-pearlitic

Surface Morphologies and Characterization

Figure 5 shows various SEM images of the surface of the specimens for the experiments with 250 rpm and 150 rpm rotational speeds removed on the 1st, 3rd and last 5th day of the experiments. The surface morphology of the 1st specimen for both rotational speed show similarities: a rough surface with no visible precipitation of $FeCO_3$. However, differences are found on specimens removed on the 3rd day as there is visible precipitation of $FeCO_3$, in the form of prismatic crystals, for the 150 rpm experiment, whereas the 250 rpm experiment still shows a bare rough steel surface with no precipitation. For the 5th day of the experiment, the surface of the specimen for the 250 rpm experiment shows some grooves on the surface and no precipitation of $FeCO_3$. However, grooves have been associated with a thick and porous layer of Fe_3C, since the ferrite phase preferentially corrodes leaving cementite behind.[3,16] The specimen for the 150 rpm experiment taken out on the 5th day shows a surface covered by $FeCO_3$ prismatic crystals, which are protective as indicated by the decrease of corrosion rate to a low and steady value as shown in Figure 4. Figure 6 shows the XRD patterns for the specimens retrieved from the 150 rpm and 250 rpm experiments after day 5. The dominant corrosion product for the 150 rpm experiment is $FeCO_3$. For the 250 rpm experiments, the corrosion products are Fe_3C and $FeCO_3$. The XRD analysis confirms the formation of $FeCO_3$ on both specimens. However, as shown by the surface morphologies and the XRD patterns, Figure 5 and Figure 6, respectively, $FeCO_3$ is more dominant on the 150 rpm specimen, which confirms that there is an effect of flow on the formation of $FeCO_3$. It is

---

[**] While the increase of corrosion rate due to buildup of Fe_3C, as detected by LPR, is real, the actual magnitude of the increase of the corrosion rate is exaggerated 2-3 times, when using this technique. This is because LPR cannot properly estimate the corrosion rate for the case of a galvanic couple with very different areas of the anode and the cathode.

also noteworthy that the corrosion product layers are sufficiently thick that no diffraction from substrate ferrite (α-Fe) is observed.
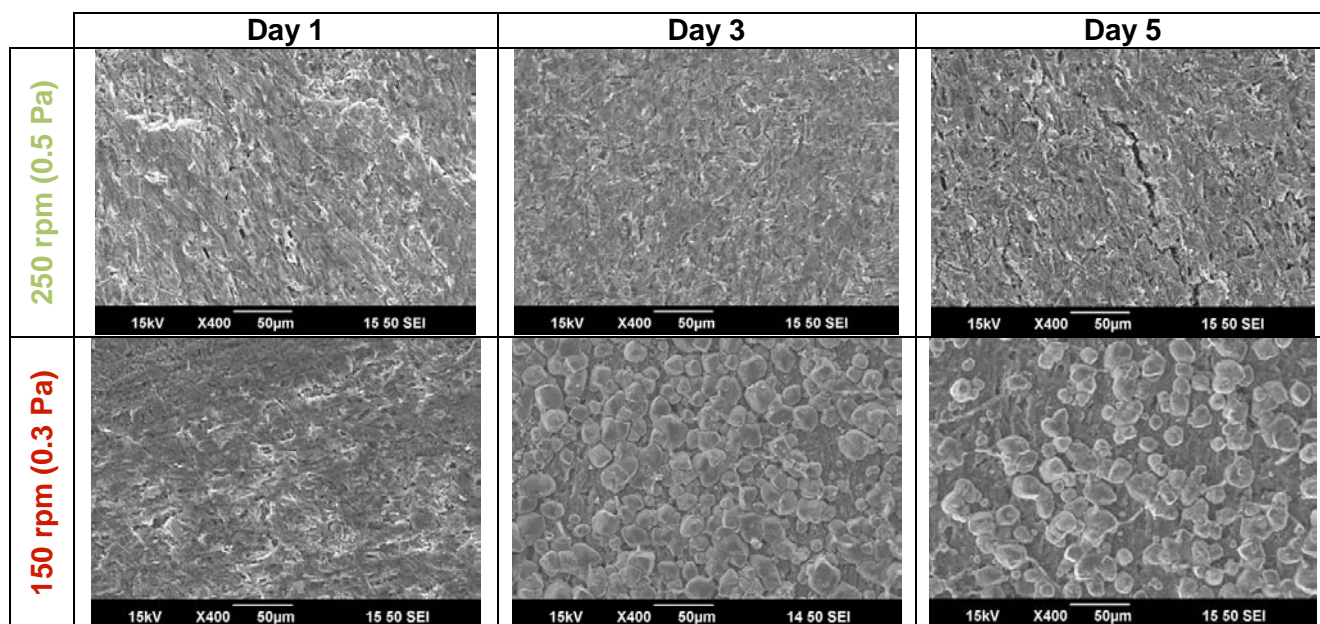

Figure 5: Comparison of surface morphologies for 150 rpm (V$_{eq}$ = 0.4 m/s, 0.3 Pa) and 250 rpm (V$_{eq}$ = 0.6 m/s, 0.5 Pa) experiments with UNS G10180 ferritic-pearlitic
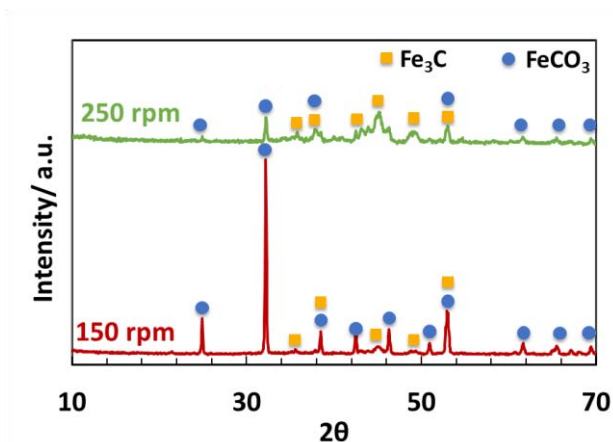

Figure 6: XRD analysis on UNS G10180 tempered martensitic specimens for 150 rpm (V$_{eq}$ = 0.4 m/s, 0.3 Pa) and 250 rpm (V$_{eq}$ = 0.6 m/s, 0.5 Pa) experiments

Cross-Sectional Morphologies

Figure 7 shows cross-section morphologies for both rotational speeds for the extracted specimens after days 1, 3, and 5. For the 1st day, it can be seen that no significant corrosion has occurred and that Fe$_3$C is only about 5 µm thick for both experiments. For the third day, a more significant Fe$_3$C network developed in both experiments. For the 150 rpm experiment after day 3, it can be observed that some FeCO$_3$ has precipitated within the porous layer of Fe$_3$C, but it does not cover the surface entirely, which is why the corrosion rate has not significantly decreased at this time, as shown in Figure 4. Finally, on day 5, the 150 rpm specimen shows that FeCO$_3$ has precipitated fully within the porous layer of Fe$_3$C. The 250 rpm specimen also shows that some precipitation occurred within the pores of Fe$_3$C but only close to the surface of the steel, which is why FeCO$_3$ prismatic crystals were not visible on the surface of the specimen, as shown in Figure 5.
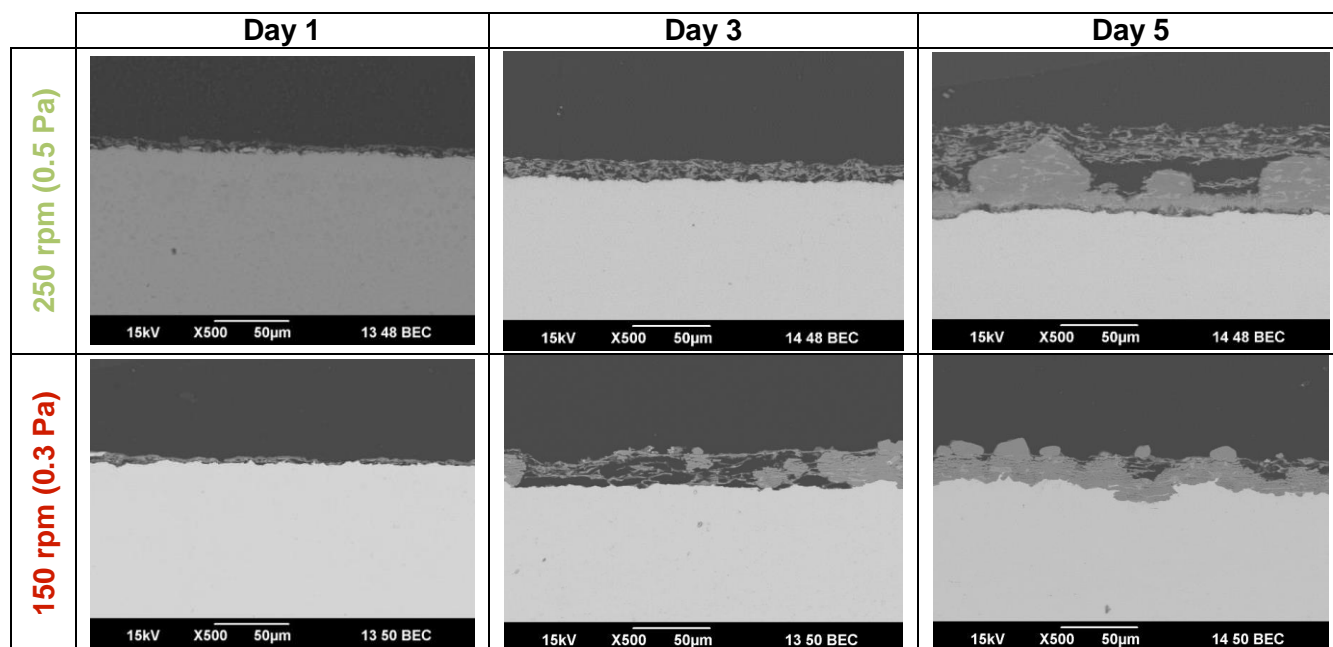
| | Day 1 | Day 3 | Day 5 |

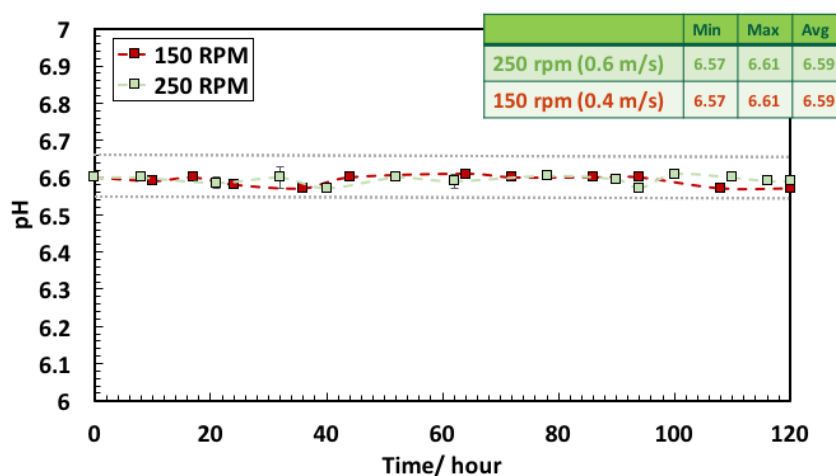**Figure 7: Comparison of cross-sectional morphologies for 150 rpm (V_{eq} = 0.4 m/s, 0.3 Pa) and 250 rpm (V_{eq} = 0.6 m/s, 0.5 Pa) experiments with UNS G10180 ferritic-pearlitic**

UNS G10180 tempered martensitic steel

Water Chemistry

Figure 8 and Figure 9 show data related to the water chemistry acquired during the course of the experiments conducted at different rotational speeds. The pH was controlled within a $\pm$0.03 range from the initial pH value of 6.60. The average pH value for both experiments was 6.59.

	Min	Max	Avg
250 rpm (0.6 m/s)	6.57	6.61	6.59
150 rpm (0.4 m/s)	6.57	6.61	6.59

Figure 8: Comparison of pH over time for 150 rpm (V_{eq} = 0.4 m/s, 0.3 Pa) and 250 rpm (V_{eq} = 0.6 m/s, 0.5 Pa) experiments with UNS G10180 tempered martensite

Figure 9 shows ferrous ion concentration at different time intervals during the course of the experiment. Even though a maximum of 7.7 ppm was obtained for the 250 rpm experiment, the average value of all data obtained was 4.0 ppm (S($FeCO_3$) $\approx$ 25), only 2.0 ppm (S($FeCO_3$) $\approx$ 10) away from the starting value. No significant changes in pH and ferrous ion concentration were observed, thus it can be concluded that environmental conditions were controlled during the experiments, with no significant deviations in supersaturation that can alter the formation of $FeCO_3$.
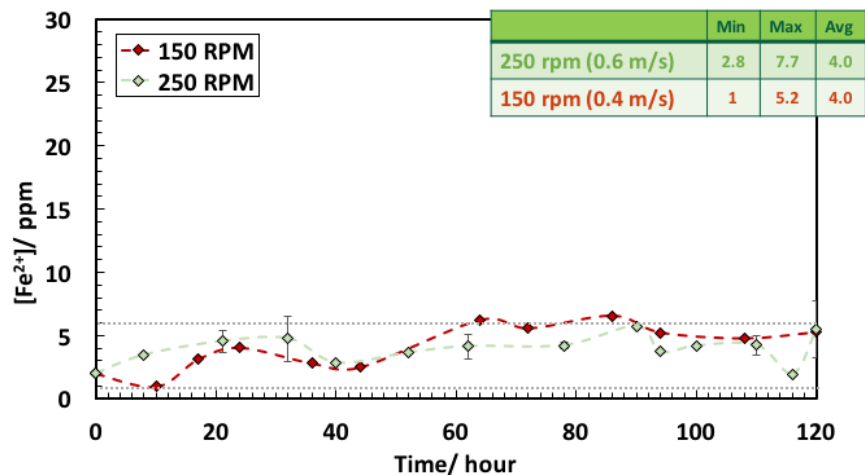
Figure 9: Comparison of [Fe^{2+}] over time for 150 rpm (V_{eq} = 0.4 m/s, 0.3 Pa) and 250 rpm (V_{eq} = 0.6 m/s, 0.5 Pa) experiments with UNS G10180 tempered martensite

Corrosion Rates

Figure 10 shows the corrosion rate measurements obtained electrochemically over time. It can be seen, similarly to the case of UNS G10180 ferritic-pearlitic, that corrosion rate increases over time. Once again, this is due to the preferential corrosion of the ferrite phase, leaving the Fe$_3$C behind which acts as a cathode.[4,6,14,15] However, unlike the UNS G10180 ferritic-pearlitic steel, where various stages of corrosion were identified in the plot of LPR corrosion rates, as shown in Figure 4 and based on previous studies,[3,5] UNS G10180 tempered martensitic steel showed only an active corrosion stage. This trend may be an indication that formation of FeCO$_3$ did not occur, since a low and steady corrosion rate was never achieved. Lastly, the corrosion rate obtained through weight loss measurements did not match the corrosion rate obtained through electrochemical measurements, similar to the findings in UNS G10180 ferritic-pearlitic, since the presence of Fe$_3$C accelerates electrochemical corrosion rates in a way that cannot be accurately measured by LPR.
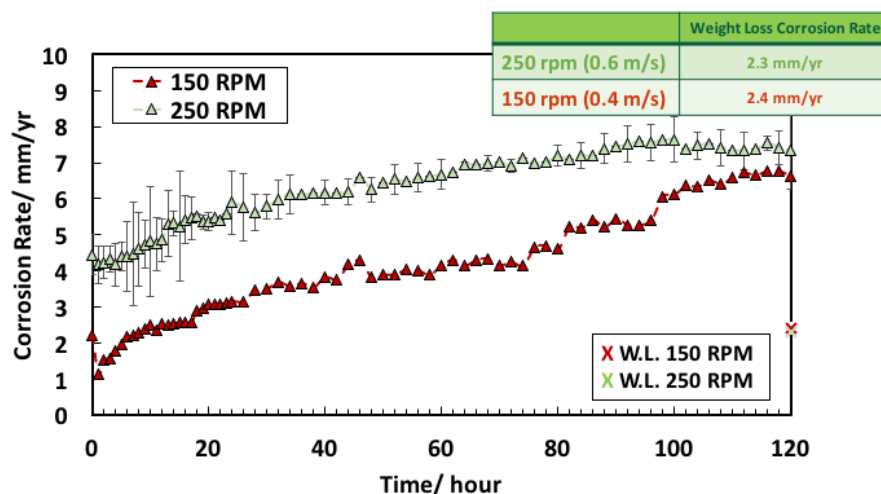

Figure 10: Comparison of LPR corrosion rate over time for 150 rpm (V_{eq} = 0.4 m/s, 0.3 Pa) and 250 rpm (V_{eq} = 0.6 m/s, 0.5 Pa) experiments with UNS G10180 tempered martensite

Surface Morphologies and Characterization

Figure 11 shows SEM images of the surface of the specimen for 250 rpm and 150 rpm experiments removed at various time intervals. The surface morphology of all specimens removed on the first day show a wrinkled surface with more defined grooves on the 250 rpm specimen than that for the 150 rpm

one. Grooves became more defined, changing their appearance to that of cracks through the course of the experiments for both rotational speeds. Although the same trend is followed in both experiments, it can be observed that the 250 rpm condition shows wider cracks than those from the 150 rpm experiment. As for the case of UNS G10180 ferritic-pearlitic, cracks are related to exposure of a Fe_3C network.[3,16] Other researchers have found that these cracks, visible by the naked eye, can appear during the drying process,[17-19] however, that was not the case for these specimens. There was no evidence of $FeCO_3$ formation, as there is no presence of prismatic-shaped crystals on the steel surface.
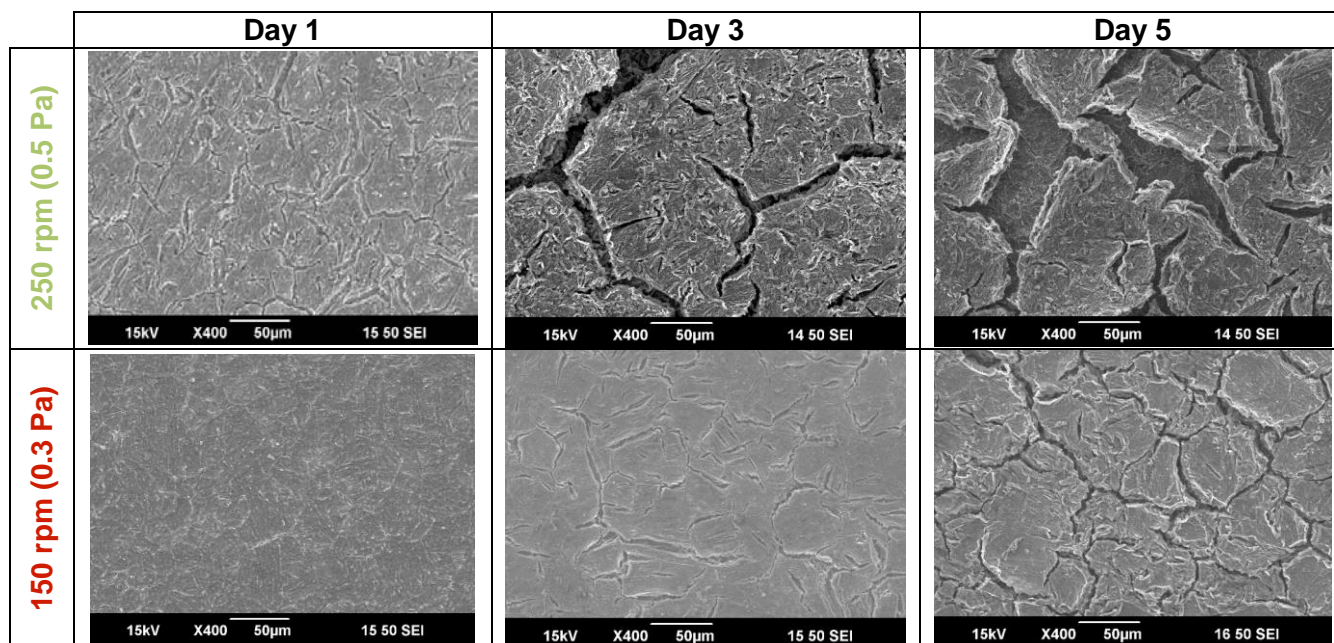

Figure 11: Comparison of surface morphologies for 150 rpm (V_{eq} = 0.4 m/s, 0.3 Pa) and 250 rpm (V_{eq} = 0.6 m/s, 0.5 Pa) experiments with UNS G10180 tempered martensite

Figure 12 shows XRD analysis done on specimens removed on the last day. Both 250 rpm 150 rpm specimens show the presence of Fe_3C and iron, and an absence of $FeCO_3$. Nonetheless, the Fe_3C peaks for the 250 rpm specimen are less pronounced than those from the 150 rpm XRD pattern. To the contrary, the substrate ferrite (α-Fe) peaks are more pronounced for the 250 rpm specimen than the 150 rpm specimen. This may be due to the thickness and compactness of the Fe_3C.
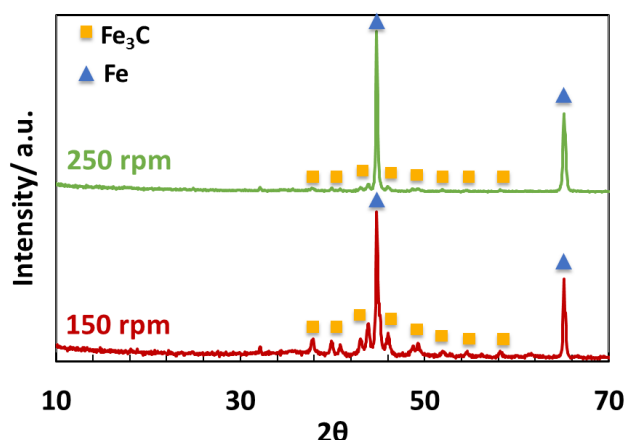

Figure 12: XRD analysis on UNS G10180 tempered martensitic specimens for 150 rpm (V_{eq} = 0.4 m/s, 0.3 Pa) and 250 rpm (V_{eq} = 0.6 m/s, 0.5 Pa) experiments

Cross-Sectional Morphologies

Figure 13 shows the cross sectional morphologies of specimens in Figure 11. After the 1st day there was no presence of corrosion product on the steel surface; no significant corrosion has occurred at this time. The cross sections from the last 5th day show some exposed Fe_3C on the surface of the specimen but no presence of $FeCO_3$ within the pores of the Fe_3C. This can be attributed to the distribution of the cementite in the material microstructure since the distribution of Fe_3C is unordered and discrete in the material microstructure; Fe_3C is more subjected to removal by flow ("weaker" Fe_3C layer), which allows for release of ferrous ions into the electrolyte without trapping them in the Fe_3C network, as opposed to what was found in a ferritic-pearlitic microstructure.
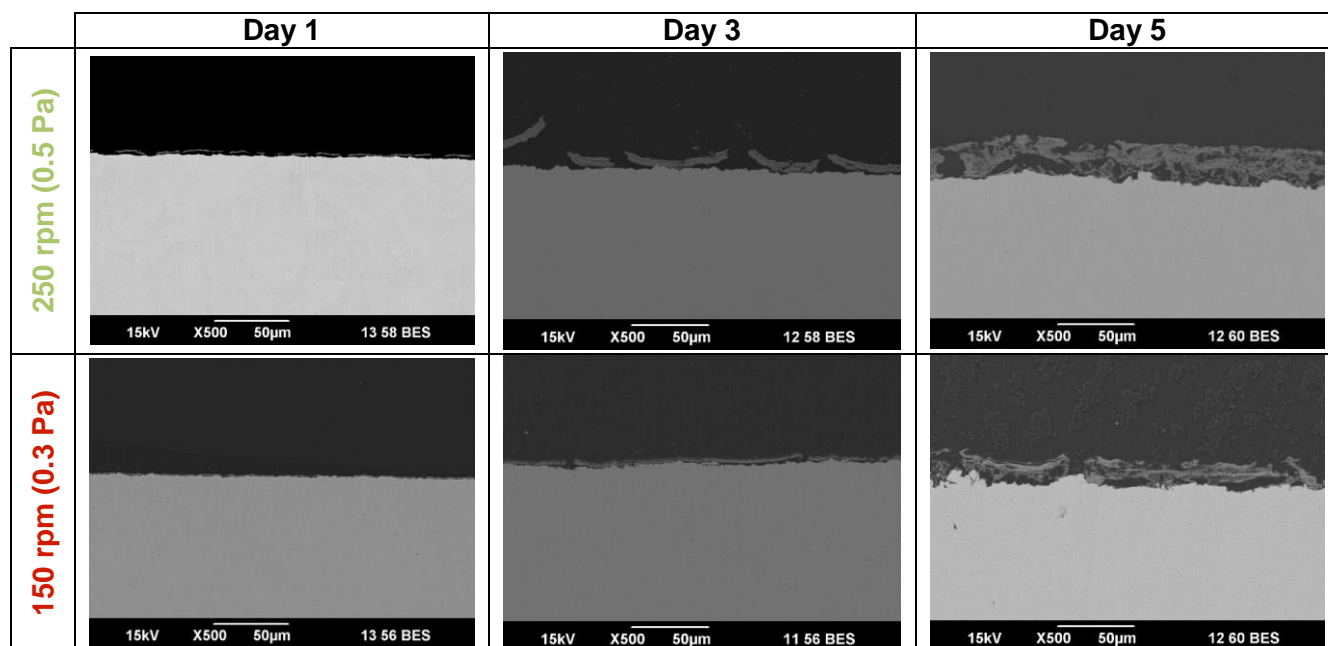

Figure 13: Comparison of cross-sectional morphologies for 150 rpm (V_{eq} = 0.4 m/s, 0.3 Pa) and 250 rpm (V_{eq} = 0.6 m/s, 0.5 Pa) experiments with UNS G10180 tempered martensite

Annealed API 5L X65 steel

Water Chemistry

Figure 14 and Figure 15 show changes in pH and ferrous ion concentration, respectively, for both rotational speeds for the entire duration of experiments. As has been the case for all materials and rotational speeds tested so far, pH values and ferrous ion concentration were well controlled and stable for all experiments over their entire duration.

Corrosion Rates

Figure 16 shows corrosion rate over time for both the 150 rpm and 250 rpm experiments. It can be seen that corrosion rates stay stable over time and do not increase, which follow a similar trend compared to reported corrosion rates of pure iron.[14] This may be associated with the fact that the carbon content of this material is low (0.05 wt.%) and the Fe_3C exposed was weak enough to be sheared away by flow and thus not affect the corrosion rate. Previously, it has been found that the carbon content does affect corrosion rate of steels, as reported in these findings.[7,22,23] Additionally, the distribution of Fe_3C also affects corrosion rate behavior;[6] however a study performed by Al-Hassan, *et al.*, concluded that there is no true effect of microstructure at temperatures above 60°C on corrosion rates,[21] which contradicts these findings, as shown in Figure 4, Figure 10, and Figure 16. Clearly, the

findings show different corrosion rate behavior depending on the microstructure and carbon content, which correlate with previous studies.[3,5,21]
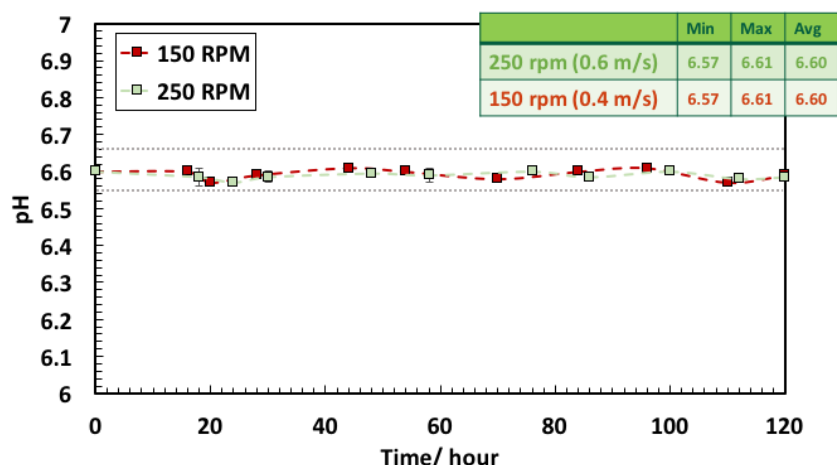

		Min	Max	Avg
250 rpm (0.6 m/s)		6.57	6.61	6.60
150 rpm (0.4 m/s)		6.57	6.61	6.60

Figure 14: Comparison of pH over time for 150 rpm (V_{eq} = 0.4 m/s, 0.3 Pa) and 250 rpm (V_{eq} = 0.6 m/s, 0.5 Pa) experiments with API 5L X65
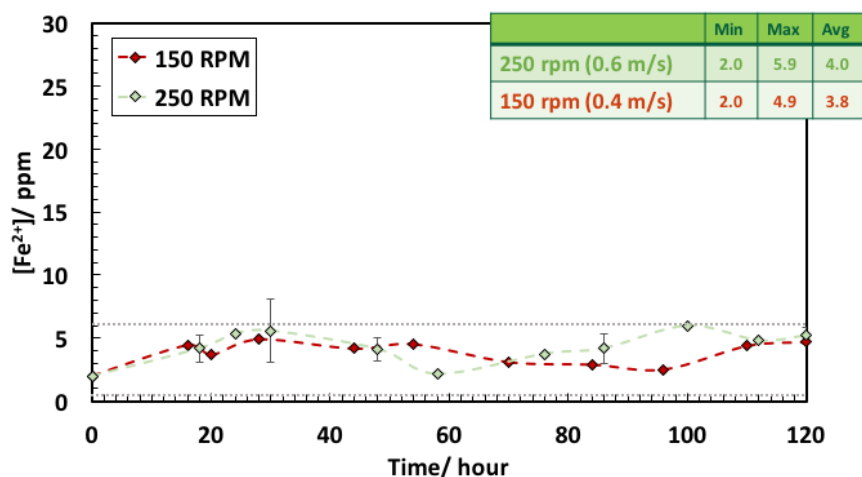

		Min	Max	Avg
250 rpm (0.6 m/s)		2.0	5.9	4.0
150 rpm (0.4 m/s)		2.0	4.9	3.8

Figure 15: Comparison of [Fe^{2+}] over time for 150 rpm (V_{eq} = 0.4 m/s, 0.3 Pa) and 250 rpm (V_{eq} = 0.6 m/s, 0.5 Pa) experiments with API 5L X65

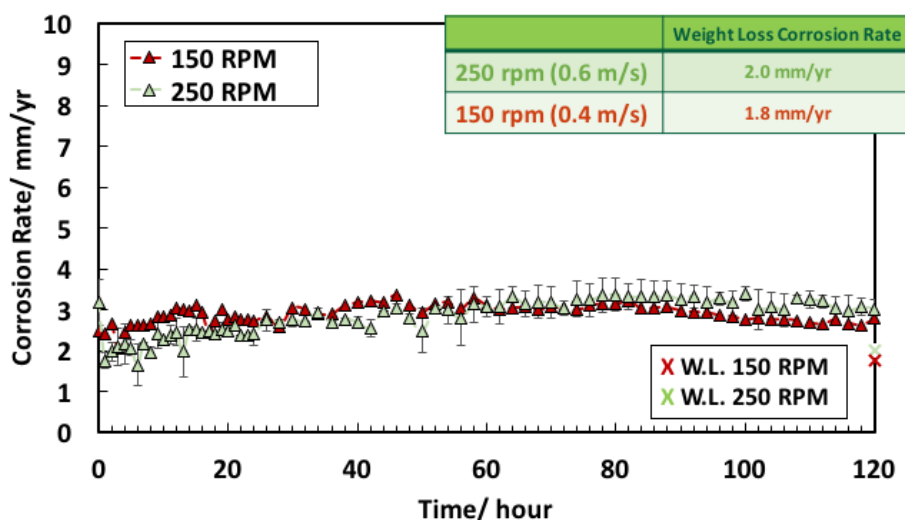|	Weight Loss Corrosion Rate
250 rpm (0.6 m/s)	2.0 mm/yr
150 rpm (0.4 m/s)	1.8 mm/yr

Figure 16: Comparison of LPR corrosion rate over time for 150 rpm (V_{eq} = 0.4 m/s, 0.3 Pa) and 250 rpm (V_{eq} = 0.6 m/s, 0.5 Pa) experiments with API 5L X65

Surface Morphologies and Characterization

Figure 17 shows the changes on surface morphology during the course of the experiment. No major differences are observed on the surface of the specimens removed after the 1st day; both specimens show a rough surface. Nevertheless, some differences are noted as grooves, which are more noticeable on the specimen retrieved from the 250 rpm experiment than from the 150 rpm experiment on the 5th day. These cracks have the same morphology as seen in previous studies, where they have been associated with Fe_3C presence.[3,16] $FeCO_3$ is absent as there are no precipitated crystals on the surface of the specimens.
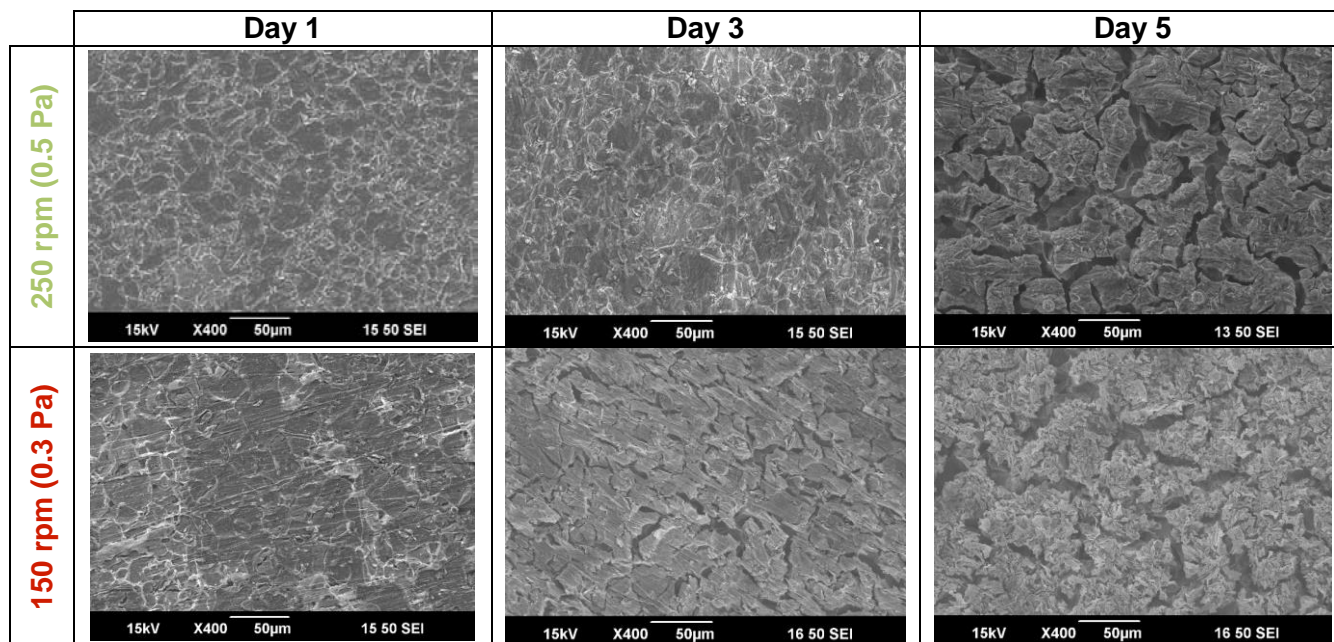

Figure 17: Comparison of surface morphologies for 150 rpm (V_{eq} = 0.4 m/s, 0.3 Pa) and 250 rpm (V_{eq} = 0.6 m/s, 0.5 Pa) experiments with API 5L X65

Figure 18 shows the XRD patterns for the surface of the specimen taken out on the 5th day of the experiment. It can be seen that only pure iron (α-Fe) peaks are present, and no corrosion products are identified, such as $FeCO_3$ and Fe_3C, indicating that Fe_3C was either never present or removed by flow, which may be due either to the low carbon content[7,22,23] or the distribution of Fe_3C.[21]
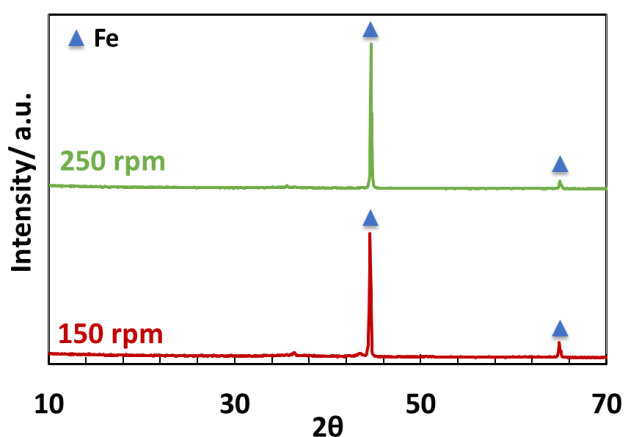

Figure 18: XRD analysis on API 5L X65 day 5 specimens for 150 rpm (V_{eq} = 0.4 m/s, 0.3 Pa) and 250 rpm (V_{eq} = 0.6 m/s, 0.5 Pa) experiments

<u>Cross-Sectional Morphologies</u>

Figure 19 shows cross-sectional morphologies of the specimens shown in Figure 17. There is no significant evidence of Fe_3C up to the first 3 days of corrosion. On the 5th day, however, a thin layer appears on the steel surface. This was confirmed by EDS to be a thin layer of Fe_3C and alloying elements. This correlates with the surface morphologies obtained by SEM, but not XRD analysis, as shown in Figure 18 since the Fe_3C is very thin and could not be detected by XRD; due to the penetration depth by incident X-rays governing magnitude of detected diffraction peaks.
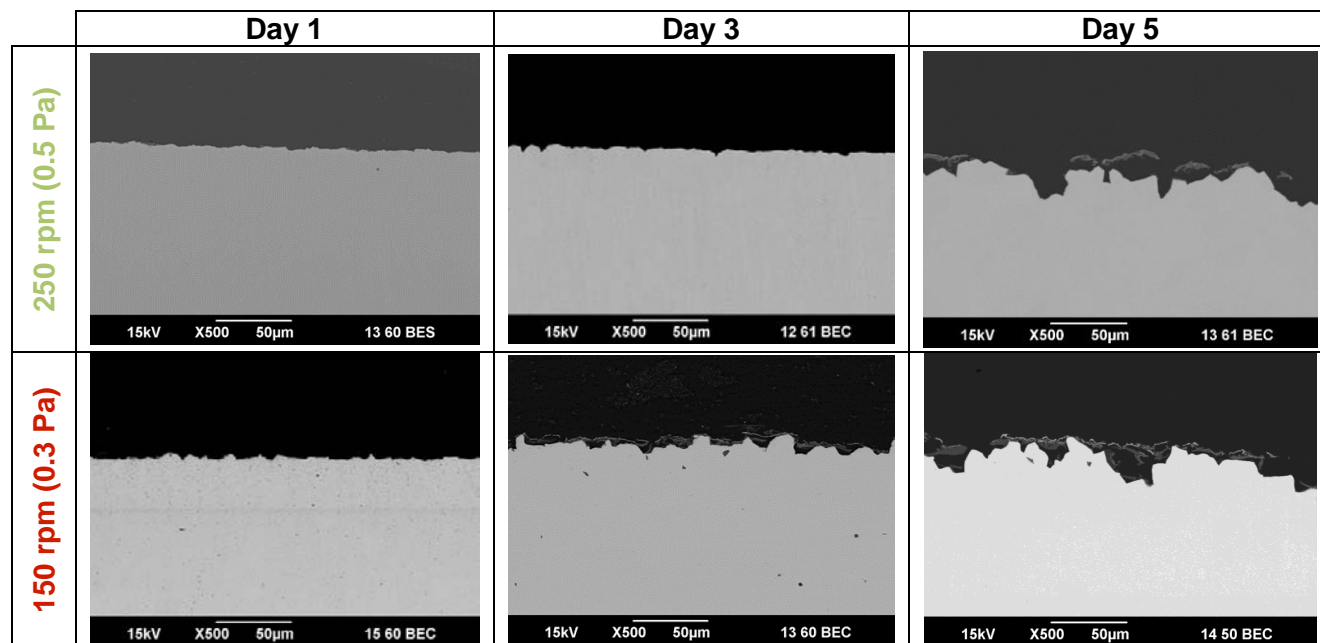

Figure 19: Comparison of cross-sectional morphologies for 150 rpm (V_{eq} = 0.4 m/s, 0.3 Pa) and 250 rpm (V_{eq} = 0.6 m/s, 0.5 Pa) experiments with API 5L X65

CONCLUSIONS

Within this context, experiments with two rotational speeds, varying microstructures and carbon content were performed in an electrochemical three-electrode glass cell setup under controlled water chemistry conditions. The results indicate that:

- Ion exchange resins used for controlling pH and ferrous ion concentration gave satisfactory results.
- Nucleation of $FeCO_3$ was significantly reduced as turbulence/flow increased even when the bulk water chemistry was favorable and the formation of Fe_3C is minimized.
- Higher carbon content, 0.18 wt.% *vs.* 0.05 wt.% C, favors precipitation of $FeCO_3$.
- Ferritic-pearlitic microstructure facilitates $FeCO_3$ precipitation due to the distribution/morphology of the Fe_3C precipitates, which enable local water chemistry conditions favorable to precipitation of $FeCO_3$.
- Flow can also impact precipitation of $FeCO_3$ due to the removal of Fe_3C from the steel surface.

ACKNOWLEDGEMENTS

their assistance in the laboratory. Ezechukwu Anyanwu is acknowledged for flow simulations to determine shear stresses.

REFERENCES

1. A. Dugstad, H. Hemmer, M. Seiersten, Effect of Steel Microstructure on Corrosion Rate and Protective Iron Carbonate Film Formation, Corrosion 57(4) p. 369.
2. N. Ochoa, C. Vega, N. Pébère, J. Lacaze, J. L. Brito, CO_2 Corrosion Resistance of Carbon Steel in Relation with Microstructure Changes, Materials Chemistry and Physics 156, p. 198
3. F. Farelas, B. N. Brown, S. Nešić, "Iron Carbide and its Influence on the Formation of Protective Iron Carbonate in CO_2 Corrosion of Mild Steel," CORROSION/2013, paper no. 2291 (Houston, TX: NACE, 2013).
4. A. Groysman, *Corrosion for Everybody* (Houten, Netherlands: Springer Netherlands).
5. S. Ieamsupapong, B. Brown, M. Singer, S. Nešić, "Effect of Solution pH on Corrosion Product Layer Formation in a Controlled Water Chemistry System," CORROSION/2017, paper no. 9160 (Houston, TX: NACE, 2017).
6. F. F. Eliyan, A. Alfantazi, On the Theory of CO_2 Corrosion Reactions Investigating their Interrelation with the Corrosion Products and API-X100 Steel Microstructure, Corrosion Science 85, p. 380.
7. T. Berntsen, M. Seiersten, T. Hemmingsen, Effect of $FeCO_3$ Supersaturation and Carbide Exposure on the CO_2 Corrosion Rate of Carbon Steel, Corrosion 69(6), p. 601.
8. Y. Sun, *Localized CO_2 Corrosion in Horizontal Wet Gas Flow Doctoral Dissertation*. (Athens, OH: Ohio University).
9. X. Zhong, B. N. Brown, W. Li, S. Nešić, M. Singer, "How to Maintain a Stable Solution Chemistry when Simulating CO_2 Corrosion in a Small Volume Laboratory System," CORROSION/2016, paper no. 7780 (Houston, TX: NACE, 2016).
10. Y. Yang, B. N. Brown, S. Nešić, "Mechanical Strength and Removal of a Protective Iron Carbonate Layer Formed on Mild Steel in CO_2 Corrosion," CORROSION/2010, paper no. 10383.
11. E. Akeer, B. N. Brown, S. Nešić, "The influence of Mild Steel Metallurgy on the Initiation of Localized CO_2 Corrosion in Flowing Conditions," CORROSION/2013, paper no. 2383 (Houston, TX: NACE, 2013).
12. R. W. Revie, H. H. Uhlig, *Uhlig's Corrosion Handbook*, 3rd ed. (Hoboken, NJ: John Wiley & Sons, 2011).
13. M. Stern, A. L. Geary, Electrochemical Polarization I. A Theoretical Analysis of the Shape of Polarization Curves, J. Electrochem.Soc. 104(1), p. 56.
14. D. N. Staicopolus, The Role of Cementite in the Acidic Corrosion of Steel, J. Electrochem. Soc. 110(11), p. 1121.
15. W. D. Callister, D. G. Rethwisch, *Materials Science and Engineering: An Introduction*, 9th ed. (New York, NY: Wiley, 2007), p. 665
16. F. Pessu, R. Barker, A. Neville, The Influence of pH on Localized Corrosion Behavior of X65 Carbon Steel in CO_2-Saturated Brines, Corrosion 71(12) p. 1452.
17. M. Singer, B. N. Brown, A. Camacho, S. Nešić, Combined Effect of Carbon Dioxide, Hydrogen Sulfide, and Acetic Acid on Bottom-of-the-Line Corrosion, Corrosion 67(1) p.15004.
18. M. Singer, A. Camacho, B. N. Brown, S. Nešić, Sour Top-of-the-Line Corrosion in the Presence of Acetic Acid, Corrosion 67(8) p. 085003.
19. M. Singer, D. Hinkson,, Z. Zhang, H. Wang, S. Nešić, CO_2 Top-of-the-Line Corrosion in Presence of Acetic Acid: A Parametric Study, Corrosion 69(7) p. 719.
20. D. Clover, B. Kinsella, B. Pejcic, R. De Marco, The Influence of Microstructure on the Corrosion Rate of Various Carbon Steels, J. Applied Electrochem. 35(2) p. 139.
21. S. Al-Hassan, B. Mishra, D. L. Olson, M. M. Salama, Effect of Microstructure on Corrosion of Steels in Aqueous Solutions Containing Carbon Dioxide, Corrosion 54(6) p. 480.
22. J. R. Vera, A. Viloria. M. Castillo, A. Ikeda, M. Ueda, Flow Velocity Effect on CO_2 Corrosion of Carbon Steel Using a Dynamic Field Tester, European Federation of Corrosion 13, p. 59.
23. A. Ikeda, M. Ueda, S. Mukai, "CO_2 Corrosion Behavior of Carbon Steel and Alloy Steel." CORROSION/1983, paper no. 45 (Houston, TX: NACE, 1983).